Revival resonant scattering, perfect caustics, and isotropic transport of pseudospin-1 particles

Hong-Ya Xu and Ying-Cheng Lai

Phys. Rev. B **94**, 165405 — Published 7 October 2016

DOI: 10.1103/PhysRevB.94.165405

Revival resonant scattering, perfect caustics and isotropic transport of pseudospin-1 particles

Hong-Ya Xu[1] and Ying-Cheng Lai[1,2,*]

[1] *School of Electrical, Computer and Energy Engineering, Arizona State University, Tempe, Arizona 85287, USA*

[2] *Department of Physics, Arizona State University, Tempe, Arizona 85287, USA*

We report drastically new physics associated with wave scattering in pseudospin-1 systems whose band structure consists of a conventional Dirac cone and a topologically flat band. First, for small scatterer size, we find a surprising revival resonant scattering phenomenon and identify a peculiar type of boundary trapping profile through the formation of unusual vortices as the physical mechanism. Second, for larger scatterer size, a perfect caustic phenomenon arises as a manifestation of the super-Klein tunneling effect, leading to the scatterer's being effectively as a Veselago lens. Third, in the far scattering field, an unexpected isotropic behavior emerges at low energies, which can be attributed to the vanishing Berry phase for massless pseudospin-1 particles and, consequently, to constructive interference between the time-reversed backscattering paths. We develop an analytic theory based on the generalized Dirac-Weyl equation to fully explain these phenomena and articulate experimental schemes with photonic or electronic systems.

PACS numbers: 03.65.Nk,03.65.Pm,03.65.Vf,03.65.Sq

I. INTRODUCTION

Solid state materials whose energy bands contain a Dirac cone structure have been an active area of research since the experimental realization of graphene[1,2]. From the standpoint of quantum transport, the Dirac cone structure and the resulting pseudospin characteristic of the underlying quasiparticles can lead to unconventional physical properties/phenomena such as high carrier mobility, anti-localization, chiral tunneling, and negative refractive index, which are not usually seen in traditional semiconductor materials. Moreover, due to the underlying physics being effectively governed by the Dirac equation, relativistic quantum phenomena such as Klein tunneling, Zitterbewegung, and pair creations can potentially occur in solid state devices and be exploited for significantly improving or even revolutionizing conventional electronics. Uncovering/developing alternative materials with a Dirac cone structure has also been extremely active[3,4]. In this regard, the discovery of topological insulators[5,6] indicates that Dirac cones with a topological origin can be created, leading to the possibility of engineering materials to generate remarkable physical phenomena such as zero-field half-integer quantum Hall effect[7], topological magneto-electric effect[8], and topologically protected wave transport[9,10].

A parallel line of research has focused on developing photonic materials with a Dirac cone structure, due to the natural analogy between electromagnetic and matter waves. For example, photonic graphene[11,12] and photonic topological insulators[13–18] have been realized, where novel phenomena of controlled light propagation have been demonstrated. Due to the much larger wavelength in optical materials as compared with the electronic wavelength, synthetic photonic devices with a Dirac cone structure can be fabricated at larger scales with greater tunabilities through modulations. The efforts have led to systems with additional features in the energy band together with the Dirac cones, opening possibilities for uncovering new and "exotic" physics with potential applications that cannot even be conceived at the present.

The materials assumed in our work are those whose energy bands consist of a pair of Dirac cones and a topologically flat band, electronic or optical. For example, in a dielectric photonic crystal, Dirac cones can be induced through accidental degeneracy that occurs at the center of the Brillouin zone. This effectively makes the crystal a zero-refractive-index metamaterial at the Dirac point where the Dirac cones intersect with another flat band[19–23]. Alternatively, configuring an array of evanescently coupled optical waveguides into a Lieb lattice[24–27] can lead to a gapless spectrum consisting of a pair of common Dirac cones and a perfectly flat middle band at the corner of the Brillouin zone. As demonstrated more recently, loading cold atoms into an optical Lieb lattice provides another experimental realization of the gapless three-band spectrum at a smaller scale with greater dynamical controllability of the system parameters[28]. With respect to creating materials whose energy bands consist of a pair of Dirac cones and a topologically flat band, there have also been theoretical proposals on Dice or $\mathcal{T}_3$ optical lattices[29–34] and electronic materials such as transition-metal oxide $SrTiO_3/SrIrO_3/SrTiO_3$ trilayer heterostructures[35], 2D carbon or MoS_2 allotropes with a square symmetry[36,37], $SrCu_2(BO_3)_2$[38] and graphene-In_2Te_2 bilayer[39].

In spite of the diversity and the broad scales to realize the band structure that consists of two conical bands and a characteristic flat band intersecting at a single point in different physical systems, there is a unified underlying theoretical framework: generalized Dirac-Weyl equation for massless spin-1 particles[31]. For convenience, we call such systems pseudospin-1 Dirac cone

systems. Comparing with the conventional Dirac cone systems with massless pseudospin/spin-1/2 quasiparticles (i.e., systems without a flat band), pseudospin-1 systems can exhibit quite unusual physics such as super-Klein tunneling for the two conical (linear dispersive) bands[23,32,40,41], diffraction-free wave propagation and novel conical diffraction[24–27], flat band rendering divergent dc conductivity with a tunable short-range disorder[42], unconventional Anderson localization[43,44], flat band ferromagnetism[28,45,46], and peculiar topological phases under external gauge fields or spin-orbit coupling[35,47–49]. Especially, the topological phases arise due to the flat band that permits a number of degenerate localized states with a topological origin (i.e., "caging" of carriers)[50]. Most existing works, however, focused on the physics induced by the additional flat band, and the scattering/transport dynamics in pseudospin-1 systems remains largely unknown (except the super-Klein tunneling behavior). Our main question is the following: what types of transport properties can arise form pseudospin-1 systems whose band structure is characterized by coexistence of a pair of Dirac cones and a flat band? To address this question in the simplest possible setting while retaining the essential physics, we study ballistic wave scattering against a circularly symmetric potential barrier. We note that for conventional Dirac cone systems with pseudospin or spin-1/2 quasiparticles, there has been extensive work on scattering[51–53] with phenomena such as caustics[54], Mie scattering resonance[55], birefringent lens[56], cloaking[57], spin-orbit interaction induced isotropic transport and skew scattering[58,59], and electron whispering gallery modes[60]. To our best knowledge, prior to our work there were no corresponding studies for pseudospin-1 Dirac cone systems.

Our main findings are three: revival resonant scattering, super-Klein tunneling induced perfect caustics, and universal low-energy isotropic transport without broken symmetries for massless quasiparticles. First, for small scatterer size, the effective three-component spinor wave exhibits revival resonant scattering as the incident wave energy is varied continuously - a phenomenon that has not been reported in any known wave systems. Strikingly, the underlying revival resonant modes show a peculiar type of boundary trapping profile in their intensity distribution. While the profile resembles that of a whispering gallery mode, the underlying mechanism is quite different: these modes occur in the wave dominant regime through the formation of fusiform vortices around the boundary in the corresponding local current patterns, rather than being supported by the gallery type of orbits through total internal reflections. Second, for larger scatterer size where the scattering dynamics are semiclassical, a perfect caustic phenomenon arises when the incident wave energy is about half of the barrier height, as a result of the super-Klein tunneling effect. A consequence is that the scatterer behaves as a lossless Veselago lens with effective negative refractive index resulting from the Dirac cone band structure. Compared with conventional Dirac cone systems for pseudospin-1/2 particles, the new caustics possess remarkable features such as significantly enhanced focusing, vanishing of the second and higher order caustics, and a well-defined static cusp. Third, in the far scattering field, an isotropic behavior arises at low energies. Considering that there is no broken symmetry so the quasiparticles remain massless, the phenomenon is quite surprising as conventional wisdom would suggest that the scattering be anisotropic. By analyzing the characteristic ratio of the transport to the elastic time as a function of the scatterer size, we find that the phenomenon of scattering isotropy can be attributed to vanishing of the Berry phase for massless pseudospin-1 particles that results in constructive interference between the time-reversed backscattering paths. Because of the isotropic structure, the emergence of a Fano-type resonance structure in the function of the ratio versus the scatterer size can be exploited to realize effective switch of wave propagation from a forward dominant state to a backward dominant one, and vice versa. We develop an analytic theory with physical reasoning to understand the three novel phenomena, and articulate experimental verification schemes with photonic or electronic systems.

II. RESULTS

We consider scattering of pseudospin-1 particle from a circularly symmetric scalar potential barrier of height V_0 defined by $V(r) = V_0\Theta(R-r)$, where R is the scatterer radius and Θ denotes the Heaviside function. The band structure for the particle consists of a pair of Dirac cones and a flat band. A comprehensive description of the Hamiltonian, its properties, the boundary conditions, and detailed solutions of the scattering waves is given in Appendix A. To characterize the scattering dynamics quantitatively, we use the scattering efficiency, defined as a ratio of the scattering to the geometric cross sections[55]:

$$Q = \frac{\sigma}{2R}, \tag{1}$$

where the scattering cross section σ can be calculated through the far field radial reflected current, as detailed in Appendix B.

A. Near-field behavior 1: Revival resonant scattering

To uncover unusual physics, we calculate and analyze the scattering efficiency Q as a function of the reduced barrier strength V_0R (normalized by the group velocity v_g associated with the Dirac cone) and the relative incident energy E/V_0. In order to highlight the unique manifestations of the unconventional band structure, we focus on the under barrier scattering process in which the particle energy is below the barrier height: $0 < E/V_0 < 1$. To be concrete, we choose $E/V_0 = 0.01, 0.1, 0.9$ and, for each

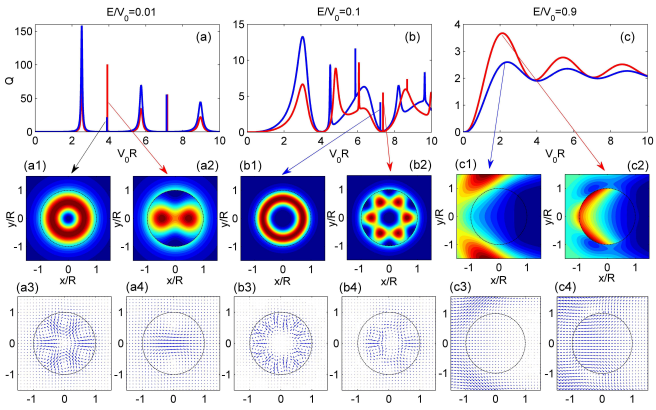

FIG. 1. **General behaviors of the scattering efficiency versus the scatterer strength**. Scattering efficiency Q as a function of the scatterer strength V_0R for a number of representative values of the relative incident energy: (a) $E/V_0 = 0.01$, (b) $E/V_0 = 0.1$, and (c) $E/V_0 = 0.9$. The middle and bottom panels show the corresponding probability density and local current density profiles, respectively. In (a-c), the blue curves are for the conventional massless pseudospin/spin-1/2 case while the red ones are for the massless pseudospin-1 wave system. Certain features can be understood by referring to the resonance width expressions $\Gamma_1 \propto (kR)^3$ for the resonances associated with the $|l| = 1$ channel and $\Gamma_0 \propto (kR) \gg \Gamma_1$ for those with the $l = 0$ channel. For example, in (a), the second and fourth modes belong to the normal excitations of the $|l| = 1$ channel, which are located about the first ($V_0R \sim 3.8$) and the second ($V_0R \sim 7$) zeros of the Bessel function J_1 in the domain of V_0R, while the first, third and fifth modes are the excitations of normal modes belonging to the $l = 0$ channel, which are located about the first (~ 2.4), the second (~ 5.5) and the third (~ 8.7) zeros of the Bessel function $J_0(V_0R)$. This is why the long lifetime (corresponding to narrow resonance width) appears in the fourth mode but not in the third and fifth modes. This argument holds in the regime $kR \ll 1$ and $E/V_0 \ll 1$.

fixed value of E/V_0, we calculate the scattering efficiency Q versus the barrier strength V_0R. For the three chosen values of E/V_0, the results are shown by the respective red curves in Figs. 1(a-c). We see that there are well-separated sharp resonances in Q for small values of E/V_0 [e.g., Fig. 1(a)], while broadened and overlapping ripple structures occur for larger values of E/V_0 [e.g., Figs. 1(b) and 1(c)]. Using the characteristic size parameter kR, we can generally classify two distinct scattering regimes: $kR \ll 1$ and $kR \gg 1$. In the former case ($kR \ll 1$), the incident wavelength $2\pi/k$ is much larger than the range R of the scattering potential. In this case, the wave effects dominate the scattering dynamics with a remarkable resonance characteristic, as shown in Figs. 1(a) and 1(b). The case $kR \gg 1$, i.e., $(1 - E/V_0)/(E/V_0)kR \gg 1$, corresponds to the semiclassical limit where the classical ray picture is applicable. In this case, the scatterer acts essentially as a Veselago reflector/lens due to an equivalent negative refractive index arising from the particular band structure of Dirac cones with a flat band.

From the explicit summation form of Q and the reflection coefficients A_l (labeled by the angular momentum l) obtained within the generalized partial-wave decomposition formalism in Appendix B, we see that the size parameter kR provides a general estimate of the maximum number of angular momentum channels contributing to the scattering process. Accordingly, we can obtain a closed form of Q in the limit of $kR \ll 1$, where only a few lowest channels dominate in a given range of the barrier strength, say $V_0R \in [0.01, 10]$. Specifically, using the short-range ($x \ll 1$) behavior of the Bessel functions appearing in the solutions of the scattering problem, we get a closed expression for the dependence of the scattering efficiency Q on the effective barrier strength V_0R for $kR \ll 1$ and $E/V_0 \ll 1$, which reads

$$Q \approx \frac{2}{kR}\left[\frac{\Gamma_0^2}{\Gamma_0^2 + \left(V_0R - x_0 + kR\ln\left(\gamma_E kR/2\right)\right)^2} + 2 \times \frac{\Gamma_1^2}{\Gamma_1^2 + \left(V_0R - x_1 - kR\right)^2}\right], \tag{2}$$

where γ_E is the constant appearing in the small value approximation of the Bessel function: $Y_0(x) \approx (2/\pi)\ln(\gamma_E x/2)$for $x \ll 1$ and the lowest $|l| = 0, 1$ channels give the leading contribution to and hence dominate the scattering process with well-separated symmetric sharp resonances around $V_0R = x_0, x_1$, which correspond to the zeros of the Bessel functions J_0 and J_1. The respective lifetimes are given by

$$\frac{1}{\Gamma_0} = \frac{2}{\pi kR} \quad \text{and} \quad \frac{1}{\Gamma_1} = \frac{2}{\pi(kR)^3}.$$

From Eq. (2), we see that, for $kR \ll 1$ and $E/V_0 \ll 1$, the resonances exhibit a Lorentzian shape (also known as the Breit-Wigner distribution). Due to their longer lifetime: $1/\Gamma_1 \gg 1/\Gamma_0$, the resonances associated with the $|l| = 1$ channel are much narrower than those with $l = 0$. In the limit $kR \to 0$, the resonant excitations are typically positioned at the zeros of $J_l(V_0R)$ with an infinite lifetime (i.e., zero resonant widths) that physically correspond to a bound state in the antidot potential profile without an incident wave. Further insights can be gained by considering the local probability and current density distributions of one particular excitation of the normal modes, e.g., the first resonance associated with the $|l| = 1$ channel, as indicated in Figs. 1(a2) and 1(a4). Analytically, we obtain the probability density inside the scattering region ($r < R$) as

$$\rho_< \approx |B_1|^2\left[J_1^2(V_0r) + \frac{J_0^2(V_0r) + J_2^2(V_0r)}{2} + \left(J_1^2 - J_0J_2\right)\cos\left(2\theta\right)\right], \tag{3}$$

together with the local current distribution

$$\begin{aligned} \boldsymbol{j}_< \approx & -\Re(B_1^* B_0)\left[2J_1^2(V_0 r) + J_0^2(V_0 r) - J_0(V_0 r)J_2(V_0 r)\right]\cos\theta \hat{e}_r \\ & + \Re(B_1^* B_0) J_0(V_0 r)\left[J_0(V_0 r) + J_2(V_0 r)\right]\sin\theta \hat{e}_\theta, \end{aligned} \tag{4}$$

where $\Re(B_1^* B_0)$ denotes the real part of $(B_1^* B_0)$, and B_l are the transmission coefficients (Appendix B). When a scattering resonance emerges, the magnitude of the transmission coefficient behaves as

$$|B_1| \sim \frac{1}{kRJ_1(V_0 R)} \gg 1,$$

leading to a noticeable probability density concentration inside the scatterer, indicating the occurrence of wave trapping/confinement. Moreover, it follows from Eq. (4) that, accompanying the confinement, a vortex pattern symmetric with respect to the $x-$axis is formed. In general, in the resonant scattering regime, the incident wave is confined/trapped in vortices (as demonstrated in the bottom panel of Fig. 1) rather than through the conventional total internal reflection mechanism.

Comparing with the conventional pseudospin-1/2 Dirac cone systems [cf., Figs. 1(a1) and 1(a3), as well as the blue curve in Fig. 1(a)], we see that there are common features in the scattering curve and trapping mechanism but with different resonant wave/current patterns. In particular, the trapping intensity distribution is radially symmetric for the pseudospin-1/2 case, but for a pseudospin-1 particle, there is an angular dependence of the scattering amplitude with a well-defined rotational symmetry, which can be analyzed for a specific resonant mode using Eq. (3).

Given the particular range of the scattering strength $V_0 R$ as set in Figs. 1(a-c), we see that increasing E/V_0 leads to larger values of kR and hence the scattering process involves higher angular momentum channels. As a result, more quasi-bound modes can be excited, generating overlapping and broadened resonances, as shown in Figs. 1(b) and 1(c). In the limit of $kR \gg 1$, say $V_0 R \gg 1$ for $E/V_0 \sim 1$, we enter the semiclassical regime where the ray picture is applicable. We obtain $Q \approx 2\left[1 - \pi\cos(2V_0 R - \pi/4)/4V_0 R\right]$ as a damped oscillatory function of the scattering strength $V_0 R$ about a constant value. Distinct from the resonant scattering regime dominated by wave interference/diffraction, in the semiclassical regime the scatterer acts as a Veselago reflector due to its effective negative refractive index. The associated local probability density and current density patterns in typical situations for both conventional massless pseudospin-1/2 and massless pseudospin-1 cases are shown in Figs. 1(b1-b4) and 1(c1-c4), respectively.

To gain further insights into the scattering behaviors, we plot Q as a function of $V_0 R$ and E/V_0, as shown in Figs. 2(a) and 2(b), respectively. As expected, for the pseudospin-1/2 Dirac cone system, the curve of Q versus $V_0 R$ tends to be smooth as E/V_0 is increased [Fig. 2(a)]. However, for the pseudospin-1 Dirac cone system shown in Fig. 2(b), the remarkable phenomenon of revival resonant scattering emerges: the sharp resonances disappear, reappear unexpectedly, and then disappear again with continuous increase in E/V_0. We emphasize that this revival phenomenon is quite exceptional which, to our knowledge, has not been reported in any other known wave systems. In the limit of $V_0 R \ll 1$ ($V_0 R > kR$), we obtain

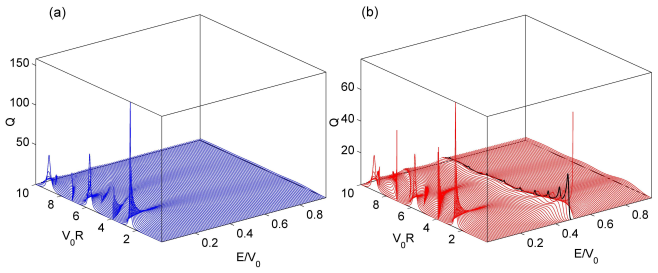

FIG. 2. **Scattering efficient Q versus the scatterer strength $V_0 R$ and the relative incident energy E/V_0** for (a) massless pseudospin-1/2 and (b) massless pseudospin-1 wave systems. The black curve is for $E/V_0 = 0.49$ with a highlighted visual effect.

$$Q \simeq \frac{2}{kR}\left[\frac{P_0^2}{P_0^2 + Q_0^2} + 2 \times \frac{P_1^2}{P_1^2 + (4 + Q_1)^2}\right], \tag{5}$$

where

$$P_0 = \pi kR, \quad \text{and}$$
$$Q_0 = 2\left[kR\ln(\gamma_E kR/2) - J_0(V_0 R - kR)/J_1(V_0 R - kR)\right],$$

with P_1 and Q_1 given by $[P_1, Q_1] = kR[P_0, Q_0]$. The first term of Eq. (5),

$$\begin{aligned} \frac{P_0^2}{P_0^2 + Q_0^2} &\approx \frac{\pi^2 J_1^2(V_0 R - kR)}{4J_0^2(V_0 R - kR)}(kR)^2 \\ &\simeq \frac{\pi^2(1 - E/V_0)^2}{16}(V_0 R)^2 (kR)^2 \ll 1, \end{aligned}$$

is off-resonance. Remarkably, the second term generates an additional resonance for $4 + Q_1 = 0$, which corresponds to the emerging revival resonance observed. Explicitly, the associated revival resonant condition can be obtained from $4 + kRQ_0 = 0$ as $E/V_0 \approx 1/2$, which agrees with the numerical results as displayed in Fig. 2(b).

Certain remarkable features of the revival resonances can be revealed through the underlying revival resonant modes (RRMs) defined in terms of the associated local probability and current density patterns. We find that the RRMs exhibit unusual boundary trapping profiles, where the higher the resonance frequency (energy) the more pronounced the trapping. Examining the corresponding local current density distribution of a specific

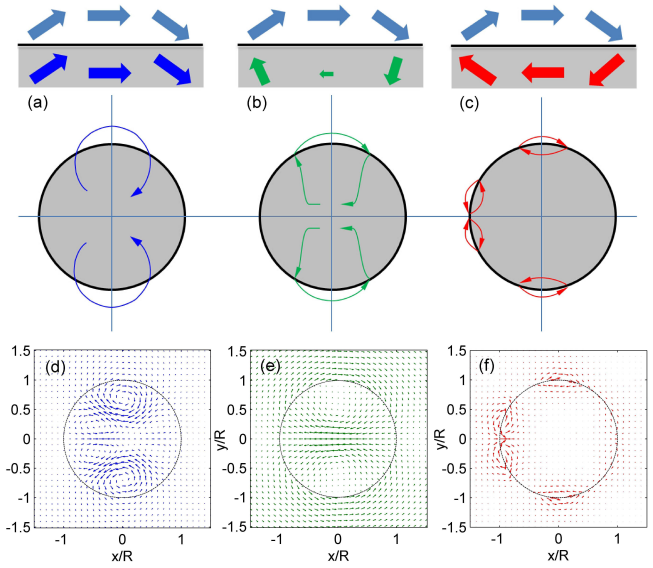

FIG. 3. **Vortex-based wave trapping for massless pseudospin-1 scattering**. (a-c) Schematic illustration of three types of vortex-based wave trapping. (d) Wave pattern near the boundary for a massless pseudospin-1/2 particle for $E/V_0 = 0.086$. (e,f) Boundary wave patterns for the massless pseudospin-1 case for $E/V_0 = 0.044$ and $E/V_0 = 0.487$, respectively. The value of V_0R is set to be 4.5 for all cases.

RRM, we find that the incident wave is fed into fusiform vortices about the boundary and is trapped there. In contrast, for conventional pseudospin-1/2 scattering, no such trapping phenomenon occurs. Using the general vortex-based trapping mechanism, we can get an intuitive physical picture for the unusual boundary trapping phenomenon through a qualitative analysis of vortex formation in the local current distribution stipulated by the boundary conditions. In particular, for a given local current configuration outside the scattering boundary, as indicated by the light blue arrows in Figs. 3(a-c), we sketch the possible local current patterns inside the boundary, denoted by the blue, green and red arrows, respectively. This can be done with the boundary conditions defined in terms of the spinor wavefunction $\Psi = [\psi_1, \psi_2, \psi_3]^T$ and their effect on the associated local current field $\boldsymbol{j}$ (see Appendix A). Since continuity is the only constraint on the normal component of the local currents at the boundary (the tangent component is in general discontinuous and can even have opposite directions), there is an additional freedom to configure the corresponding current pattern inside the potential region for a particular pattern outside. This leads to the remarkable fusiform boundary vortices as illustrated in Fig. 3(c) with the dramatic phenomenon of boundary trapping and, consequently, to the resonances in the curve of the scattering efficiency. Note that, for the conventional scalar or spinor wave systems, the current configuration is well-determined in the sense that, given a configuration on one side of the boundary, that on the other side is then determined completely. This is due to the continuity in both components of the local currents at the boundary, as illustrated in Fig. 3(a). As a concrete example, we demonstrate the full local current patterns in Figs. 3(d-f), where the former two represent the typical local current profiles underlying the conventional low-order resonant modes excited in the massless pseudospin-1/2 and massless pseudospin-1 wave systems, respectively, while the last one is for that of the RRM that arises only for the massless pseudospin-1 wave system.

For pseudospin-1 Dirac cone systems, a remarkable phenomenon is super-Klein tunneling (see Appendix A), which occurs when the energy of the incident particle is about one half of the potential height. In this case, forward scattering is maximized. In contrast, the revival scattering resonances are associated with fusiform vortices about the boundary, creating perfect wave trappings there and eliminating any forward scattering. Both super-Klein tunneling and revival resonant scattering depend on the scatterer strength V_0R and the relative incident energy E/V_0. From an applied point of view, it is thus possible to switch the super-Klein-tunneling dominant forward scattering on and off efficiently by tuning the parameters. In fact, the higher pseudospin degree of freedom and the flexible scattering boundary conditions render richer current patterns that can be manipulated through parameter perturbation. This may find applications in novel photonic integrated circuit design, as pseudospin-1 systems have been realized experimentally in a variety of photonic crystals[19,20,23–26,28].

While the RRMs uncovered appear similar to the well-known whispering gallery modes (WGMs) in terms of the intensity profiles, we emphasize that the underlying mechanisms are quite different. In particular, the WGMs are due to the total internal reflection within an effective semiclassical ray regime, but the RRMs result from the formation of unusual, dominant vortices locally attached to the boundary due to wave interference and can thus occur for much smaller scatterer size kR, a regime in which the semiclassical ray approximation fails. An explicit comparison of conventional resonant, revival resonant and whispering gallery modes for the pseudospin-1 Dirac cone system is presented in Fig. 4.

B. Near-field behavior 2: perfect caustics

Caustics, a spatial region in which the density of light rays is singular, occur in the semiclassical regime. This phenomenon is quite common in daily life, mostly through geometric optics. For a pseudospin-1/2 Dirac cone system, caustics can occur due to the tunable effective negative refractive index and the Klein tunneling effect, as shown in Figs. 5(a) and 5(c). For the pseudospin-1 Dirac cone system, the surprising phenomenon of perfect caustic/lens behavior occurs, as shown in Figs. 5(b) and 5(d) for the same parameter as in Figs. 5(a) and 5(c), which emerges in the regime where the incident wave-

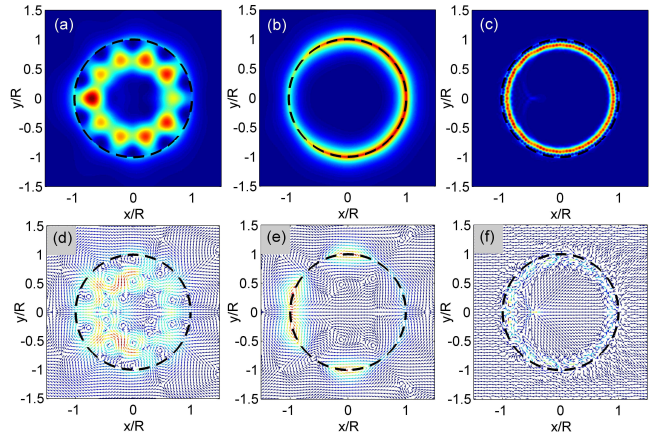

FIG. 4. **Comparision of conventional resonant, revival resonant and whispering gallery modes for pseudospin-1 Dirac cone system**. (a-c): Typical probability distributions for the conventional resonant mode (CRM), revival resonant mode (RRM) and whispering gallery mode (WGM), respectively, where the scattering parameters $[E/V_0, V_0R]$ are: (a) [0.2, 11.598], (b) [0.487,4.5] and (c) [0.4157, 100]. (d-f) The corresponding current patterns.

length is much smaller than the scatterer radius R. The caustic patterns for the massless pseudospin-1 system are "perfect" in the sense that they are significantly more focused/concentrated than the pseudospin-1/2 counterparts. We find that perfect caustics are a result of the super-Klein tunneling effect for massless pseudospin-1 particle, where the transmission coefficient approaches unity for *any* incident angle[23,32,40,41]. Specifically, for a single straight scattering interface, we obtain the transmission coefficient for incident angle θ $(-\pi/2 \le \theta \le \pi/2)$ as

$$T = \frac{4\tau\tau' \cos\theta' \cos\theta}{\cos^2\theta' + \cos^2\theta + 2\tau\tau' \cos\theta' \cos\theta}, \tag{6}$$

with the refractive angle given by

$$\theta' = \pi - \tan^{-1} \frac{|E/V_0| \sin\theta}{\sqrt{(1 - E/V_0)^2 - (E/V_0)^2 \sin^2\theta}},$$

where $\tau = \mathrm{sgn}(E)$ and $\tau' = \mathrm{sgn}(E - V_0)$. It follows from Eq. (6) that $T \equiv 1$ for $E/V_0 = 1/2$, regardless of the incident angle, as shown by the thick red curve in Fig. 6, signifying a super-Klein tunneling behavior. For comparison, the incident angle dependent transmission probability for the conventional pseudospin-1/2 system is shown as the thick blue line in the same figure.

Within the ray formalism and based on differential geometry[54], we obtain analytically the following caustic envelope equation defining a curve $\boldsymbol{r}_c = (x_c, y_c)$ as

$$\frac{\boldsymbol{r}_c(p,\theta)}{R} = (-)^{p-1} \left[(-\cos\Theta, \sin\Theta) + \cos\beta \frac{1 + 2(p-1)\beta'}{1 + (2p-1)\beta'} \times (\cos(\Theta + \beta), -\sin(\Theta + \beta)) \right], \tag{7}$$

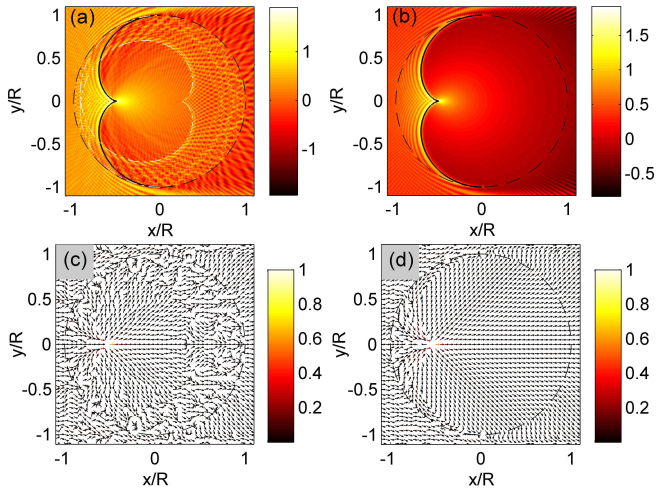

FIG. 5. **Caustic behavior in the semiclassical regime and perfect caustics in pseudospin-1 Dirac cone systems**. The probability and local current density patterns, respectively, for (a,c) conventional pseudo-1/2 and (b,d) pseudospin-1 Dirac cone systems. The probability density patterns in (a) and (b) are plotted on a logarithmic scale. The corresponding local current density patterns in (c) and (d) are color-coded with magnitude normalized by its maximum. The parameters are $kR = 300$ and $E/V_0 = 1/2$.

where $\Theta = \theta + 2(p-1)\beta$, $\sin\beta = \sin\theta/|1 - V_0/E|$, and $\beta' = \cos\theta/\sqrt{(1 - V_0/E)^2 - \sin^2\theta}$ with p being the number of chords inside the scattering region corresponding to $p-1$ internal reflections. Intuitively, the caustics for $p > 1$ are less visible since the ray intensity decreases after each internal reflection. However, for our pseudospin-1 Dirac cone system, the super-Klein tunneling effect for $E/V_0 = 1/2$ will suppress the $p > 1$ caustics completely, leading to a perfect caustic for $p = 1$, which intuitively can be better seen from the corresponding local current patterns in Figs. 5(c,d).

While super-Klein tunneling $T \equiv 1$ occurs exactly for $E/V_0 = 0.5$ for the entire range of the incident angle, even when E/V deviates from the value of 0.5 (e.g., $E/V = 0.4$), $T \approx 1$ still persists for a substantial range of the incident angle, as shown in the top-right corner of Fig. 7. In addition, the phenomenon of perfect caustics holds as well, as shown in Figs. 7(b,d). Because of the flexible energy range for super-Klein tunneling and perfect caustics to occur, it may be feasible to observe these phenomena in experiments.

C. Far-field behavior: isotropic scattering of massless pseudospin-1 quasiparticles and control

Far away from the scattering center, i.e., $r \gg R$, for unit incident density, the spinor wavefunction can be

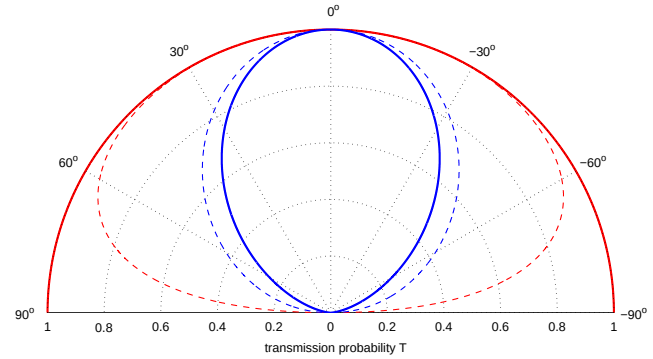

FIG. 6. **Super-Klein tunneling in pseudospin-1 Dirac cone systems**. Transmission probability: red and blue curves are for the massless pseudospin-1 and pseudospin-1/2 particles, respectively, with $E/V_0 = 0.5$ (solid lines) and $E/V_0 = 0.4$ (dash lines). For the former (solid red line) the transmission is unity, regardless of the incident angle.

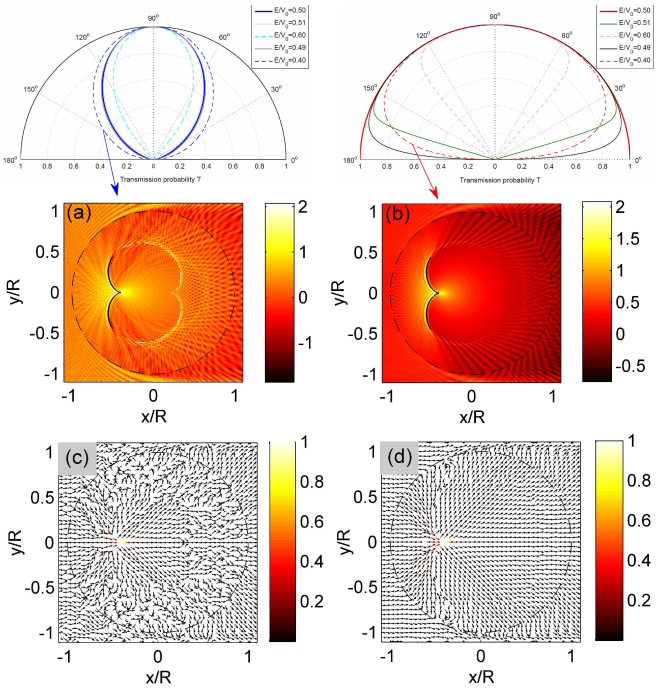

FIG. 7. **Robustness of super-Klein tunneling and perfect caustics in pseudospin-1 Dirac cone systems**. Top panels: polar plots of the transmission probability for different values of E/V_0 as indicated. The left column is for the pseudospin-1/2 system, while the right is for the pseudospin-1 system. Parameters used for generating the caustic patterns are $kR = 300$ and $E/V_0 = 0.4$ (rather than exactly at $E/V_0 = 0.5$).

written as

$$\Psi_>(r,\theta) \approx \frac{1}{2}\begin{pmatrix} 1 \\ \sqrt{2}\tau \\ 1 \end{pmatrix} e^{ikr\cos\theta} + \frac{1}{2}\begin{pmatrix} e^{-i\theta} \\ \sqrt{2}\tau \\ e^{i\theta} \end{pmatrix} \frac{f(\theta)}{\sqrt{r}} e^{ikr}, \tag{8}$$

where $f(\theta)$ denotes the 2D far-field scattering amplitude in the direction defined by the angle θ with the x axis. The differential and the total cross sections are given, respectively, by

$$\frac{\mathrm{d}\sigma}{\mathrm{d}\theta} = |f(\theta)|^2, \tag{9}$$

and

$$\sigma = \int_0^{2\pi} |f(\theta)|^2 \mathrm{d}\theta. \tag{10}$$

In addition, we define the transport or momentum-relaxation cross section as

$$\sigma_{\rm tr} = \int_0^{2\pi} \mathrm{d}\theta |f(\theta)|^2 (1-\cos\theta). \tag{11}$$

The three types of cross sections are experimentally measurable and can be used to quantitatively characterize the basic scattering and transport physics for pseudospin-1 Dirac cone systems. For example, consider such a system with randomly distributed identical scatterers of low concentration, i.e., $n_c \ll 1/R^2$, the conductivity in units of the conductance quantum G_0 can be expressed as (see Appendix C)

$$\frac{G}{G_0} = \frac{k}{n_c \sigma_{\rm tr}} = v_g k \tau_{\rm tr}, \tag{12}$$

where the sample size is assumed to be larger than the mean-free path $L = v_g\tau_{\rm tr}$ with $\tau_{\rm tr}$ being the transport mean free time, and v_g is the group velocity. The elastic scattering time (the quantum lifetime) τ_e can be determined from the total cross section through

$$\frac{1}{\tau_e} = n_c v_g \sigma. \tag{13}$$

The two time scales define the following characteristic ratio:

$$\xi = \frac{\tau_{\rm tr}}{\tau_e} = \frac{\sigma}{\sigma_{\rm tr}} \equiv \frac{\oint \mathrm{d}\theta |f(\theta)|^2}{\oint \mathrm{d}\theta |f(\theta)|^2 (1-\cos\theta)}, \tag{14}$$

which can be used to characterize the far-field behavior of the scattering process. Through a detailed analysis, we obtain the following formula (see Appendix B):

$$\xi = \frac{2\sum_l \sin^2\delta_l}{\sum_l \sin^2(\delta_{l+1}-\delta_l)}, \tag{15}$$

where δ_l is the scattering phase shift associated with angular momentum l.

We present our finding of the general isotropic nature of low-energy scattering for massless pseudospin-1 wave. To be concrete, we calculate from Eq. (15) the ratio ξ as a function of kR for a given barrier strength $V_0R = 5$. The result is shown as the red curves in Fig. 8, where we see that there is a characteristic constant ratio $\xi \approx 1$ of the transport time to the elastic time for

$kR \ll 1$. For comparison, we calculate the corresponding ratio for the massless pseudospin-1/2 wave, where low-energy scattering is universally anisotropic as characterized by the constant ratio $\xi \approx 2$[53,58]. Our result indicates that, for a massless pseudospin-1 particle, back scattering is as pronounced as forward scattering. This finding is quite counterintuitive as, if the massless nature of the quasiparticles is sustained, they can penetrate through potential barriers of arbitrary strength via the mechanism of Klein tunneling, making forward scattering more pronounced. Since super-Klein tunneling can occur for massless pseudospin-1 quasiparticles but the scattering is isotropic at low energies, the message is that, to generate isotropic transport, it may not be necessary to break symmetries to alter the massless nature of the quasiparticles through, e.g., additional mechanisms such as spin-orbit interactions. Equivalently, an isotropic ratio ξ for massless quasiparticles does not necessarily imply any symmetry breaking leading to a finite mass.

To gain deeper insights into the physics underlying the counterintuitive phenomenon of isotropic scattering for massless particles, we analyze the characteristic ratio ξ in terms of the scattering cross sections. The reflection coefficient associated with angular momentum l satisfies $A_l = A_{-l}$. Using this relation, we obtain the differential cross section as (Appendix B)

$$\frac{\mathrm{d}\sigma}{\mathrm{d}\theta} = \frac{2}{\pi k}\{|A_0|^2 + 2\sum_{n=1}^{\infty}|A_n|^2[1+\cos(2n\theta)] + 4\sum_{n=1}^{\infty}\Re(A_0A_n^*)\cos(n\theta) + 8\sum_{m>n=1}^{\infty}\Re(A_nA_m^*)\cos(n\theta)\cos(m\theta)\}. \tag{16}$$

In the regime $kR \ll 1$ where the total angular momentum channels ($l = 0, \pm 1$) dominate the scattering process, we have

$$\frac{\mathrm{d}\sigma}{\mathrm{d}\theta} \approx \frac{2}{\pi k}\left\{|A_0|^2 + 2|A_1|^2[1+\cos(2\theta)]\right\}, \tag{17}$$

resulting in an isotropic ratio that agrees with the simulation result:

$$\xi \equiv \frac{\oint \mathrm{d}\theta \frac{d\sigma}{d\theta}}{\oint \mathrm{d}\theta \frac{d\sigma}{d\theta}(1-\cos\theta)} \approx 1. \tag{18}$$

A remarkable feature associated with the expression of $\mathrm{d}\sigma/\mathrm{d}\theta$ in Eq. (17) is the presence of backscattering characterized by a finite differential cross section at $\theta = \pi$:

$$\left.\frac{\mathrm{d}\sigma}{\mathrm{d}\theta}\right|_{\theta=\pi} = \frac{2}{\pi k}\left[|A_0|^2 + 4|A_1|^2\right], \tag{19}$$

which results from the constant term contributed by the $l = 0$ channel and the constructive interference between the time-reversed scattering paths denoted by $l = \pm 1$. The underlying physical picture can then be understood, as follows. Consider the pseudohelicity defined as $\hat{h} = \boldsymbol{S}\cdot\boldsymbol{k}/k$. Its eigenvalues are conserved during the scattering process because of the commutation $[\hat{h}, \hat{H}] = 0$ for the massless pseudospin-1 system. In general, when time-reversal symmetry is taken into account, a typical backscattering process consists of a pair scattering paths with a 2π relative rotation of the pseudospin between them. This leads to a phase difference determined by the underlying Berry phase $e^{i\Phi_B}$. For a massless pseudospin-1 particle, we have $\Phi_B = 0$. There is thus coherent interference for backscattering, which makes the low-energy scattering isotropic. When this general picture is applied to a conventional pseudospin-1/2 Dirac cone system with $\Phi_B = \pi$, it is straightforward to see that, for backscattering there is complete destructive interference and the zero total angular momentum channel is absent[51,61]. In particular, we have, for the differential cross section, $\mathrm{d}\sigma/\mathrm{d}\theta \sim (1+\cos\theta)$ for $kR \ll 1$. The ratio ξ thus becomes $\xi \approx 2/\oint \mathrm{d}\theta(1-\cos 2\theta) = 2$. The analysis agrees with the numerical results in Fig. 8.

Another phenomenon is the emergence of Fano-like resonance profile for larger values of kR where higher angular momentum channels can be excited and interfere with the lower ones, as manifested in the behavior of ξ versus kR. This provides a way to manipulate Klein-tunneling based scattering. In particular, for the conventional pseudospin-1/2 Dirac cone system (as illustrated by the blue curves in the insets (II) and (III) of Fig. 8), the preferred scattering directions can be controlled through tuning of the quantity kR. However, for such particles, since backscattering is typically totally suppressed, it is not possible to switch between forward and backward scattering. Remarkably, controlled switching in the scattering dynamics from forward to backward and vice versa can be done for our pseudospin-1 system. There are in fact a number of controllable scattering scenarios ranging from the isotropic type ($\xi \approx 1$), the backscattering dominant type ($\xi < 1$), and the forward scattering dominant type ($\xi > 2$), and the switches among them can be realized by tuning the scattering parameter kR. The feasibility of controlled scattering can be seen from the red curves in the insets of Fig. 8. This capability of scattering control can have potential applications in unconventional photonic/electronic circuit design.

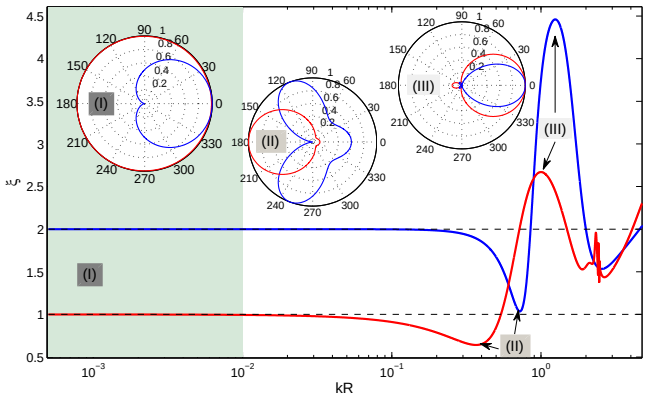

FIG. 8. **Isotropic scattering of massless pseudospin-1 quasiparticle**. Ratio ξ as a function of kR for $V_0R = 5$: the red and blue lines are for the massless pseudospin-1 and pseudospin-1/2 cases, respectively.

III. DISCUSSION

Using a general Hamiltonian for pseudospin-1 systems whose energy band structure constitutes a pair of Dirac cones and a topologically flat band, we investigate the basic problem of wave scattering from a circularly symmetric potential barrier. In spite of its simplicity, the system gives unusual and unexpected physics: revival resonant scattering, perfect caustics, and isotropic scattering for massless quasiparticles. In particular, for small scatterer size, the effective three-component spinor wave exhibits revival resonant (Mie) scattering features as the incident wave energy is varied continuously - a surprising phenomenon which, to our knowledge, has not been reported in any known wave systems. For larger scatter size rendering semiclassical the underlying scattering dynamics, a super-caustic phenomenon arises when the incident wave energy is about half of the barrier height, which is essentially a manifestation of the super-Klein tunneling effect for massless pseudospin-1 particles. Because of Klein tunneling, intuitively wave scattering should be anisotropic due to suppression of backward scattering, which is indeed the case for conventional pseudospin-1/2 particles. However, for a pseudospin-1 particle, the associated Berry phase can lead to constructive interference in the backward direction, leading to the counterintuitive phenomenon of isotropic scattering even for massless quasiparticles. We develop an analytic theory and physical understanding with extensive numerical support to substantiate our findings.

It is possible to conduct experimental test of the findings of this paper. For example, in a recent work[23], it was demonstrated for a class of two-dimensional dielectric photonic crystals with Dirac cones induced accidentally[19–22] that the Maxwell's equations can lead to an effective Hamiltonian description sharing the same mathematical structure as that of massless pseudospin-1 particles. Especially, the photonic analogy of the gate potential in the corresponding electronic system can be realized by manipulating the scaling properties of Maxwell's equations. Recent experimental realizations of photonic Lieb lattices consisting of evanescently coupled optical waveguides implemented through the femtosecond laser-writing technique[24–27] make them prototypical for studying the physics of pseudopsin-1 Dirac systems. With a particular design of the refractive index profile across the lattice to realize the scattering configuration, our findings can be experimentally tested. Loading ultracold atoms into an optical Lieb lattice fabricated by interfering counter-propagating laser beams[28] provides another versatile platform to test our findings, where appropriate holographic masks can be used to implement the desired scattering potential barrier[32,62]. In electronic systems, we note that the historically studied but only recently realized 2D magnetoplasmon system[63] is described by three-component linear equations with the same mathematical structure of massless pseudospin-1 particles, which can serve as a 2D electron gas system to test our results.

From an applied perspective, the phenomenon of revival resonant scattering can be a base for articulating a new class of microcavity lasers based on the principles of relativistic quantum mechanics. It may also lead to new discoveries in condensed matter physics through exploiting the phenomenon in electronic systems. The phenomenon of perfect caustics can have potential applications in optical imaging defying the diffraction limit as well as in optical cloaking.

ACKNOWLEDGEMENTS

This work was supported by ONR under Grant No. N00014-16-1-2828 and by AFOSR under Grant No. FA9550-15-1-0151.

Appendix A: Hamiltonian and general properties

The effective low-energy Hamiltonian associated with pseudospin-1 Dirac cones can be written, in the unit $\hbar = 1$, as[23,24,40]

$$H_0 = v_g \boldsymbol{S}\cdot\boldsymbol{k}, \tag{A1}$$

where v_g is the magnitude of the group velocity associated with the Dirac cone, $\boldsymbol{k} = (k_x, k_y)$ denotes the wavevector, and $\boldsymbol{S} = (S_x, S_y)$ is a vector of matrices with components

$$S_x = \frac{1}{\sqrt{2}}\begin{pmatrix} 0 & 1 & 0 \\ 1 & 0 & 1 \\ 0 & 1 & 0 \end{pmatrix} \quad \text{and} \quad S_y = \frac{1}{\sqrt{2}}\begin{pmatrix} 0 & -i & 0 \\ i & 0 & -i \\ 0 & i & 0 \end{pmatrix}. \tag{A2}$$

Along with another matrix

$$S_z = \begin{pmatrix} 1 & 0 & 0 \\ 0 & 0 & 0 \\ 0 & 0 & -1 \end{pmatrix},$$

the three matrices form a complete representation of spin-1, which satisfies the angular momentum commutation relations $[S_l, S_m] = i\epsilon_{lmn}S_n$ with three eigenvalues: $s = \pm 1, 0$, where ϵ_{lmn} is the Levi-Civita symbol. It follows from Eq. (A1) that the energy spectrum consists of three bands that intersect at the Dirac point: a dispersionless flat band $E_0(\boldsymbol{k}) = 0$ and two linearly dispersive bands $E_\tau(\boldsymbol{k}) = \tau v_g|\boldsymbol{k}|$ with $\tau = \pm 1$ being the band index. The corresponding eigenfunctions in the position representation $\boldsymbol{r} = (x, y)$ are

$$\psi_{\boldsymbol{k},\tau}(\boldsymbol{r}) = \langle \boldsymbol{r}|\boldsymbol{k}, \tau\rangle = \frac{1}{2}\left[e^{-i\theta}, \sqrt{2}\tau, e^{i\theta}\right]^T e^{i\boldsymbol{k}\cdot\boldsymbol{r}}, \quad \text{(A3)}$$

for the dispersive bands and

$$\psi_{\boldsymbol{k},0}(\boldsymbol{r}) = \langle \boldsymbol{r}|\boldsymbol{k}, 0\rangle = \frac{1}{\sqrt{2}}\left[-e^{-i\theta}, 0, e^{i\theta}\right]^T e^{i\boldsymbol{k}\cdot\boldsymbol{r}}, \quad \text{(A4)}$$

for the flat band, where $\theta = \tan^{-1}(k_y/k_x)$. The current operator is defined from Eq. (A1) as

$$\hat{\boldsymbol{j}} = \nabla_{\boldsymbol{k}} H_0 = v_g \boldsymbol{S}. \quad \text{(A5)}$$

The local current in a given state $\psi(\boldsymbol{r}) = [\psi_1, \psi_2, \psi_3]^T$ can thus be expressed as

$$\begin{aligned} \boldsymbol{j}(\boldsymbol{r}) &= v_g \psi^\dagger \boldsymbol{S}\psi \equiv (j_x, j_y) \\ &= \sqrt{2}v_g\left(\Re[\psi_2^*(\psi_1 + \psi_3)], -\Im[\psi_2^*(\psi_1 - \psi_3)]\right), \end{aligned} \quad \text{(A6)}$$

which satisfies the common continuity equation

$$\frac{\partial}{\partial t}\rho + \nabla \cdot \boldsymbol{j} = 0, \quad \text{(A7)}$$

where $\rho = \psi^\dagger\psi$ is the probability density associated with state ψ. From Eqs. (A3) and (A4), we see that the associated local current density satisfies $\boldsymbol{j}_0 = \boldsymbol{0}$ for the flat band plane-wave, and

$$\boldsymbol{j}_\tau = v_g(\cos\theta, \sin\theta) = \tau v_g \frac{\boldsymbol{k}}{|\boldsymbol{k}|}, \quad \text{(A8)}$$

for the dispersive band plane-wave. In terms of the Berry phase associated with the band structure, we obtain from Eqs. (A3) and (A4) the corresponding Berry connections

$$\begin{aligned} \mathcal{A}^\tau_{\boldsymbol{k}} &= \langle \boldsymbol{k}, \tau|i\nabla_{\boldsymbol{k}}|\boldsymbol{k}, \tau\rangle = 0, \\ \mathcal{A}^0_{\boldsymbol{k}} &= \langle \boldsymbol{k}, 0|i\nabla_{\boldsymbol{k}}|\boldsymbol{k}, 0\rangle = -2\mathcal{A}^\tau_{\boldsymbol{k}} = 0 \end{aligned}$$

for all three bands. The Berry phase is thus given by

$$\Phi_B^{\tau,0} = \oint_{\mathcal{C}^{\tau,0}_{\boldsymbol{k}_d}} d\boldsymbol{k} \cdot \mathcal{A}^{\tau,0}_{\boldsymbol{k}} = 0, \quad \text{(A9)}$$

for any closed path $\mathcal{C}^{\tau,0}_{\boldsymbol{k}_d}$ encircling the degeneracy point $\boldsymbol{k}_d$ of the momentum space defined in each band. We note that the vanishing or 2π quantized Berry phase is consistent with the fundamental properties of spin-1 particles.

Super-Klein tunneling. A remarkable phenomenon for pseudospin-1 Dirac cone systems, which is not usually seen in conventional Dirac cone systems such as graphene and topological insulators, is super-Klein tunneling[23]. Specifically, following the standard treatment of Klein tunning for graphene systems[64], one can consider the basic problem of wave scattering from a rectangular scalar (electrostatic) potential barrier defined as $V(x, y) = V_0\Theta(x)\Theta(D - x)$ with barrier width D and height V_0. The transmission probability based on the effective Hamiltonian Eq. (A1) for incident energy $E \neq 0, V_0$ is given by

$$T = \frac{(1-\gamma^2)(1-\gamma'^2)}{(1-\gamma^2)(1-\gamma'^2) + \frac{1}{4}(\gamma+\gamma')^2\sin^2(q_x D)}, \quad \text{(A10)}$$

where $\gamma = \tau\sin\theta$, $\gamma' = \tau'\sin\theta'$ with $\tau = \text{sgn}(E)$, $\tau' = \text{sgn}(E - V_0)$, $\theta = \tan^{-1}(k_y/k_x)$ is the incident angle, and $\theta' = \arctan(k_y/q_x)$ with

$$q_x = \sqrt{(E - V_0)^2 - k_y^2}.$$

A striking feature of Eq. (A10) is that, when the incident wave energy is one half of the potential barrier height, i.e., $E = V_0/2$, one has $\tau = -\tau', \theta = \theta'$ and, consequently, perfect transmission with $T \equiv 1$ for *any* incident angle θ - hence the term "super-Klein tunneling."

Appendix B: Analysis of scattering of massless pseudospin-1 wave

Due to the circular symmetry of the scattering potential, it is convenient to formulate the solution in the polar coordinates $\boldsymbol{r} = (r, \theta)$, in which the Hamiltonian is

$$\hat{H} = \hat{H}_0 + V(r)\mathbf{1} = \frac{v_g}{\sqrt{2}}\begin{pmatrix} 0 & \hat{L}_- & 0 \\ \hat{L}_+ & 0 & \hat{L}_- \\ 0 & \hat{L}_+ & 0 \end{pmatrix} + V_0\Theta(r - R)\mathbf{1}, \quad \text{(B1)}$$

with the compact operator given by

$$\hat{L}_\pm = -ie^{\pm i\theta}\left(\partial_r \pm i\frac{\partial_\theta}{r}\right).$$

The z component of the total angular momentum is $\hat{J}_z = -i\partial_\theta + \hat{S}_z$, and we have $[\hat{H}, \hat{J}_z] = 0$. For a conventional two-dimensional Dirac cone system with massless spin-1/2 excitations, we have

$$\begin{aligned} &\begin{pmatrix} 0 & \hat{L}_- \\ \hat{L}_+ & 0 \end{pmatrix}\begin{pmatrix} f_l^{(0,1)}(kr) \\ i\tau f_{l+1}^{(0,1)}(kr)e^{i\theta} \end{pmatrix} e^{il\theta} \\ &\qquad = E\begin{pmatrix} f_l^{(0,1)}(kr) \\ i\tau f_{l+1}^{(0,1)}(kr)e^{i\theta} \end{pmatrix} e^{il\theta}, \end{aligned} \quad \text{(B2)}$$

where the radial function $f_l^{(0)} = J_l$ is the Bessel's function, and $f_l^{(1)} = H_l^{(1)}$ is the Hankel's function of the first

kind. Assuming $V_0 = 0$, we obtain solutions to Eq. (B1):

$$\psi_{lE}^{(0,1)}(r,\theta) = \frac{1}{\sqrt{2\pi}} \begin{pmatrix} f_{l-1}^{(0,1)}(kr)e^{-i\theta} \\ i\tau\sqrt{2} f_l^{(0,1)}(kr) \\ -f_{l+1}^{(0,1)}(kr)e^{i\theta} \end{pmatrix} e^{il\theta}, \tag{B3}$$

for the dispersive band $E = \tau v_g k$, and

$$\psi_{l0}^{(0,1)}(r,\theta) = \frac{1}{\sqrt{2\pi}} \begin{pmatrix} f_{l-1}^{(0,1)}(kr)e^{-i\theta} \\ 0 \\ f_{l+1}^{(0,1)}(kr)e^{i\theta} \end{pmatrix} e^{il\theta} \tag{B4}$$

for the flat band $E = 0$. Apparently, ψ_{lE} and ψ_{l0} act as a spinor spherical wave basis for massless spin-1 excitation governed by Hamiltonian (A1). To reveal and characterize the basic scattering features/mechanisms in a massless pseudospin-1 Dirac cone system, we turn on the circularly symmetric scattering potential $V(r) = V_0\Theta(R-r)$ and launch an incident plane spinor wave of a massless spin-1 particle outside the scattering region ($r > R$). Without loss of generality, we assume that the incident wave propagating along the x axis with a finite incident energy $|E| > 0$ is explicitly given by

$$\psi_{k,\tau}^{I}(r,\theta) = \frac{1}{2} \begin{pmatrix} 1 \\ \sqrt{2}\tau \\ 1 \end{pmatrix} e^{ikr\cos\theta}. \tag{B5}$$

Making use of the Jacobi-Anger identity

$$e^{iz\cos\theta} \equiv \sum_{l=-\infty}^{\infty} i^l J_l(z) e^{il\theta},$$

we can rewrite the incident wave in the spinor spherical wave basis as

$$\begin{aligned} \psi_{k,\tau}^{I}(r,\theta) &= \frac{1}{2}\sum_l i^{l-1} \begin{pmatrix} J_{l-1}e^{i(l-1)\theta} \\ i\tau\sqrt{2}J_l e^{il\theta} \\ -J_{l+1}e^{i(l+1)\theta} \end{pmatrix} \\ &= \sqrt{\frac{\pi}{2}} \sum_{l=-\infty}^{\infty} i^{l-1}\psi_{lE}^{(0)}(r,\theta). \end{aligned} \tag{B6}$$

Since the total (pseudo-)angular momentum is conserved during scattering, the reflected wave can be written as ($r > R$)

$$\psi_{k,\tau}^{R}(r,\theta) = \sqrt{\frac{\pi}{2}} \sum_{l=-\infty}^{\infty} i^{l-1} A_l \psi_{lE}^{(1)}(r,\theta). \tag{B7}$$

Similarly, we define the transmitted wave inside the scattering region ($r < R$) as

$$\psi_{q,\tau'}^{T}(r,\theta) = \sqrt{\frac{\pi}{2}} \sum_{l=-\infty}^{\infty} i^{l-1} B_l \psi_{lE'}^{(0)}(r,\theta), \tag{B8}$$

where $q = |E - V_0|/v_g$ and $E' = E - V_0 = \tau' v_g q$. The total wavefunction outside the scattering region ($r > R$) is given by

$$\Psi_{>}(r,\theta) = \psi_{k,\tau}^{I}(r,\theta) + \psi_{k,\tau}^{R}(r,\theta) = [\psi_1^{>}, \psi_2^{>}, \psi_3^{>}]^T, \tag{B9}$$

while the wavefunction inside the scattering region ($r < R$) is

$$\Psi_{<}(r,\theta) = \psi_{q,\tau'}^{T}(r,\theta) = [\psi_1^{<}, \psi_2^{<}, \psi_3^{<}]^T. \tag{B10}$$

In order to determine the reflection and transmission coefficients, A_l and B_l, respectively, we need the exact boundary conditions (BCs) imposed on the total wave functions at the scattering interface ($r = R$).

Boundary conditions for massless pseudospin-1 scattering. Recalling the commutation relation $[\hat{J}_z, \hat{H}] = 0$ (i.e., conservation of the total angular momentum), we define the following wavefunction

$$\Psi(r,\theta) = [\psi_1, \psi_2, \psi_3]^T = \begin{pmatrix} \mathcal{R}_1(r)e^{-i\theta} \\ \mathcal{R}_2(r) \\ \mathcal{R}_3(r)e^{i\theta} \end{pmatrix} e^{il\theta}, \tag{B11}$$

which satisfies

$$\hat{H}\Psi = E\Psi. \tag{B12}$$

Substituting Eq. (B11) into Eq. (B12) and eliminating the angular components, we obtain the following one-dimensional, first-order ordinary differential equation for the radial component of the wavefunction:

$$\begin{aligned} -i\frac{v_g}{\sqrt{2}} \begin{pmatrix} 0 & \frac{d}{dr}+\frac{l}{r} & 0 \\ \frac{d}{dr}-\frac{l-1}{r} & 0 & \frac{d}{dr}+\frac{l+1}{r} \\ 0 & \frac{d}{dr}-\frac{l}{r} & 0 \end{pmatrix} \begin{pmatrix} \mathcal{R}_1(r) \\ \mathcal{R}_2(r) \\ \mathcal{R}_3(r) \end{pmatrix} \\ = [E - V(r)] \begin{pmatrix} \mathcal{R}_1(r) \\ \mathcal{R}_2(r) \\ \mathcal{R}_3(r) \end{pmatrix}. \end{aligned} \tag{B13}$$

Directly integrating the radial equation over a small interval $r \in [R-\eta, R+\eta]$ defined about the interface at $r = R$ and taking the limit $\eta \to 0$, we obtain

$$\begin{aligned} \mathcal{R}_2(R-\eta) &= \mathcal{R}_2(R+\eta), \\ \mathcal{R}_1(R-\eta) + \mathcal{R}_3(R-\eta) &= \mathcal{R}_1(R+\eta) + \mathcal{R}_3(R+\eta), \end{aligned} \tag{B14}$$

provided that the potential $V(r)$ and the radial wavefunction components $\mathcal{R}_{1,2,3}(r)$ are all finite. Reformulating the continuity conditions in terms of the corresponding wavefunctions, we obtain the boundary conditions for scattering of massless pseudospin-1 wave as

$$\begin{aligned} \psi_2^{<}(R,\theta) &= \psi_2^{>}(R,\theta), \\ \psi_1^{<}(R,\theta)e^{i\theta} + \psi_3^{<}(R,\theta)e^{-i\theta} &= \psi_1^{>}(R,\theta)e^{i\theta} + \psi_3^{>}(R,\theta)e^{-i\theta}. \end{aligned} \tag{B15}$$

It follows from Eq. (B15) that in general there is a discontinuity in the spinor components ψ_1 and ψ_3.

To see the physical meaning underlying the boundary conditions, we calculate the associated local current density in a given state $\Psi = [\psi_1, \psi_2, \psi_3]^T$, which in the polar coordinates reads

$$\begin{cases} j_r = v_g \Psi^\dagger \boldsymbol{S} \cdot \hat{e}_r \Psi = \sqrt{2} v_g \Re\left[\psi_2^* \left(\psi_1 e^{i\theta} + \psi_3 e^{-i\theta}\right)\right], \\ j_\theta = v_g \Psi^\dagger \boldsymbol{S} \cdot \hat{e}_\theta \Psi = -\sqrt{2} v_g \Im\left[\psi_2^* \left(\psi_1 e^{i\theta} - \psi_3 e^{-i\theta}\right)\right], \end{cases} \tag{B16}$$

where $\hat{e}_r = (\cos\theta, \sin\theta)$ and $\hat{e}_\theta = (-\sin\theta, \cos\theta)$. We conclude from Eq. (B16) that the boundary conditions in Eq. (B15) imply conservation/continuity of the radial (normal) current density j_r across the boundary, but the angular (tangent) current density j_θ needs not to be continuous across the boundary in general. In addition, with respect to the probability density $\rho = |\psi_1|^2+|\psi_2|^2+|\psi_3|^2$, we infer from the boundary conditions the following two features: (1) $\rho_< \neq \rho_>$ in general (2) a larger probability density difference $\Delta\rho = \rho_< - \rho_>$ will occur if there is a prominent imbalance in the wavefunction components between ψ_1 and ψ_3 across the boundary. For the closed scattering boundary studied in this paper, we have $\rho_< = |\mathcal{R}_1^<|^2 + |\mathcal{R}_2^<|^2 + |\mathcal{R}_3^<|^2$ and $\rho_> = |\mathcal{R}_1^>|^2 + |\mathcal{R}_2^>|^2 + |\mathcal{R}_3^>|^2$. Making use of the boundary conditions in Eq. (B14), we obtain

$$\Delta\rho = \left(|\mathcal{R}_1^<|^2 + |\mathcal{R}_3^<|^2\right) - \left(|\mathcal{R}_1^>|^2 + |\mathcal{R}_3^>|^2\right), \tag{B17}$$

with the constraint $\mathcal{R}_1^< + \mathcal{R}_3^< = \mathcal{R}_1^> + \mathcal{R}_3^> \equiv 2\overline{\mathcal{R}}$. Defining δ as the (radial) wavefunction component imbalance strength and then substituting

$$\mathcal{R}_1^< = \overline{\mathcal{R}} - \delta_<, \mathcal{R}_3^< = \overline{\mathcal{R}} + \delta_<; \mathcal{R}_1^> = \overline{\mathcal{R}} - \delta_>, \mathcal{R}_3^> = \overline{\mathcal{R}} + \delta_>$$

into Eq. (B17), we obtain

$$\Delta\rho = 2\left(\delta_<^2 - \delta_>^2\right). \tag{B18}$$

As a result, we see that there is a remarkable increase in the probability density, $\Delta\rho \sim 2\delta_<^2$, from the outer to the interior of the scattering boundary if the scattering potential redistributes the wavefunction components such that $|\delta_<| \gg |\delta_>| \sim 0$, suggesting the emergence of a strong boundary confinement/trapping phenomenon.

Imposing the boundary conditions on the total wavefunctions on both sides of the scattering region as in Eqs. (B9) and (B10), we get

$$\begin{cases} B_l J_l(qR) = \tau\tau' \left[J_l(kR) + A_l H_l^{(1)}(kR)\right], \\ B_l X_l^{(0)}(qR) = X_l^{(0)}(kR) + A_l X_l^{(1)}(kR), \end{cases} \tag{B19}$$

where

$$X_l^{(0,1)} = f_{l-1}^{(0,1)} - f_{l+1}^{(0,1)}.$$

Solving Eq. (B19), we obtain the reflection and transmission coefficients, respectively, as

$$A_l = -\frac{J_l(qR)X_l^{(0)}(kR) - \tau\tau' X_l^{(0)}(qR)J_l(kR)}{J_l(qR)X_l^{(1)}(kR) - \tau\tau' X_l^{(0)}(qR)H_l^{(1)}(kR)}, \tag{B20}$$

$$B_l = \frac{H_l^{(1)}(kR)X_l^{(0)}(kR) - X_l^{(1)}(kR)J_l(kR)}{H_l^{(1)}(kR)X_l^{(0)}(qR) - \tau\tau' X_l^{(1)}(kR)J_l(qR)}. \tag{B21}$$

The θ-independent expressions of A_l and B_l are consistent with the rotational symmetry of the system. Using the basic relations $J_{-l} = (-)^l J_l$ and $H_{-l}^{(1)} = (-)^l H_l^{(1)}$, we have $A_{-l} = A_l$ and $B_{-l} = B_l$. Once A_l and B_l have been obtained, the resulting probability density $\rho = \Psi^\dagger\Psi$ and the local current density $\boldsymbol{j} = v_g\Psi^\dagger \boldsymbol{S}\Psi$ can be calculated.

Scattering efficiency. To quantify the scattering dynamics of massless pseudospin-1 particle, we use the scattering efficiency in terms of the scattering cross section as $Q = \sigma/(2R)$. In general, the various scattering cross sections can be calculated using the far field radial reflected current. For example, for the incident wave given in Eq. (B5), we have $\sigma = 1/(\tau v_g)\int_{-\pi}^{\pi} j_\infty^{\rm ref} r d\theta$ with $j_\infty^{\rm ref} \equiv \lim_{r\to\infty} j_r^{\rm ref}(\theta)$ being the far-field radial reflected current. We have

$$j_r^{\rm ref}(\theta) = \frac{\tau v_g}{2}\Re\left\{\sum_{l,m} i^{m-l-1} A_l^* A_m H_l^{(2)}(kr)\left[H_{m-1}^{(1)}(kr) - H_{m+1}^{(1)}(kr)\right]e^{i(m-l)\theta}\right\}. \tag{B22}$$

With the asymptotic expressions of the Hankel functions $H_l^{(1,2)}(kr) \sim \sqrt{[2/(\pi kr)]}e^{\pm i(kr - l\frac{\pi}{2} - \frac{\pi}{4})}$ for $kr \gg 1$, we have

$$j_\infty^{\rm ref} \sim \frac{2\tau v_g}{\pi kr}\Re\left[\sum_{l,m} A_l^* A_m e^{i(m-l)\theta}\right], \tag{B23}$$

and finally arrive at

$$\sigma = \frac{4}{k}\sum_{l=-\infty} |A_l|^2, \tag{B24}$$

and

$$Q = \frac{2}{kR}\sum_{l=-\infty}^{\infty} |A_l|^2 = \frac{2}{kR}\left(|A_0|^2 + 2\sum_{n=1}^{\infty}|A_n|^2\right). \tag{B25}$$

Far-field behavior: general analysis. Far away from the scattering center, i.e., $r \gg R$, for unit incident density, the spinor wavefunction can be written as

$$\Psi_>(r,\theta) \approx \frac{1}{2}\begin{pmatrix} 1 \\ \sqrt{2}\tau \\ 1 \end{pmatrix} e^{ikr\cos\theta} + \frac{1}{2}\begin{pmatrix} e^{-i\theta} \\ \sqrt{2}\tau \\ e^{i\theta} \end{pmatrix} \frac{f(\theta)}{\sqrt{r}} e^{ikr}, \tag{B26}$$

where $f(\theta)$ denotes the 2D far-field scattering amplitude in the direction defined by angle θ with the x axis. The differential and the total cross sections are given, respectively, by

$$\frac{\mathrm{d}\sigma}{\mathrm{d}\theta} = |f(\theta)|^2, \tag{B27}$$

and

$$\sigma = \int_0^{2\pi} |f(\theta)|^2 \mathrm{d}\theta. \tag{B28}$$

In addition, we define the transport or momentum-relaxation cross section as

$$\sigma_{\mathrm{tr}} = \int_0^{2\pi} \mathrm{d}\theta |f(\theta)|^2 (1-\cos\theta). \tag{B29}$$

The three types of cross sections are experimentally measurable and can be used to quantitatively characterize the basic scattering and transport physics for pseudospin-1 Dirac cone systems. For example, consider such a system with randomly distributed identical scatterers of low concentration, i.e., $n_c \ll 1/R^2$, the conductivity in units of the conductance quantum G_0 can be expressed as

$$\frac{G}{G_0} = \frac{k}{n_c\sigma_{\mathrm{tr}}} = v_g k \tau_{\mathrm{tr}}, \tag{B30}$$

where the sample size is assumed to be larger than the mean-free path $L = v_g\tau_{\mathrm{tr}}$ with τ_{tr} being the transport mean free time. The elastic scattering time (the quantum lifetime) τ_e can be determined from the total cross section through

$$\frac{1}{\tau_e} = n_c v_g \sigma. \tag{B31}$$

The ratio of the two characteristic times defines the following pertinent dimensionless parameter

$$\xi = \frac{\tau_{\mathrm{tr}}}{\tau_e} = \frac{\sigma}{\sigma_{\mathrm{tr}}} \equiv \frac{\oint \mathrm{d}\theta |f(\theta)|^2}{\oint \mathrm{d}\theta |f(\theta)|^2 (1-\cos\theta)}, \tag{B32}$$

leading to insights into the type and the spatial structure of the impurities presented in the sample. In particular, long-range impurities have a large value of ξ, while a small value implies that the impurities are short-ranged or have sharp boundaries. Equation (B32) can be used to measure the degree of angular anisotropy of the scattering process. In fact, a recent work[58] demonstrated that there is a general constant $\xi \approx 2$ characterizing the anisotropic feature of low-energy scattering for massless pseudospin-1/2 wave in the presence of short-range scatterers, while the spin-orbit interactions that make the quasiparticles massive can dramatically change this scenario, effectively leading to an isotropic ratio of $\xi \approx 1$ - a typical signature of scattering of massive particles at low energies. More recently, the angular scattering feature for a general α-T_3 model was studied[65], and an explicit relation between ξ and the underlying Berry phase Φ_B was obtained with the finding that massless pseudospin-1 wave (i.e., for $\Phi_B = 0$) possesses the much larger ratio of $\xi = 3$. These results imply that scattering of massless pseudospin-1 wave should be much more anisotropic than the massless pseudospin-1/2 wave, due to super-Klein tunneling. However, we find that this may not be true for massless pseudospin-1 wave in general. In contrast, the underlying low-energy scattering displays a remarkable isotropic character (i.e., $\xi \approx 1$) even without any symmetry breaking affecting the massless nature of the quasiparticle.

From the exact expression of $\Psi_>$ [Eq. (B9)], we obtain the scattering amplitude in terms of the reflection coefficients A_l as

$$f(\theta) = e^{-i\frac{\pi}{4}}\sqrt{\frac{2}{\pi k}}\sum_{l=-\infty}^{\infty} A_l e^{il\theta} = \frac{e^{-i\pi/4}}{\sqrt{2\pi k}}\sum_{l=-\infty}^{\infty}(S_l - 1)e^{il\theta}, \tag{B33}$$

where

$$S_l \equiv 1 + 2A_l = -\frac{J_l(qR)\left[H_{l-1}^{(2)}(kR) - H_{l+1}^{(2)}(kR)\right] - \tau\tau'\left[J_{l-1}(qR) - J_{l+1}(qR)\right]H_l^{(2)}(kR)}{J_l(qR)\left[H_{l-1}^{(1)}(kR) - H_{l+1}^{(1)}(kR)\right] - \tau\tau'\left[J_{l-1}(qR) - J_{l+1}(qR)\right]H_l^{(1)}(kR)} = e^{2i\delta_l}, \tag{B34}$$

with δ_l denoting the scattering phase shift associated with angular momentum l. Substituting the expression

of $f(\theta)$ into Eqs. (B27)-(B29), we obtain the differential cross section as

$$\frac{\mathrm{d}\sigma}{\mathrm{d}\theta} = \frac{1}{2\pi k}\left|\sum_l (S_l - 1)e^{il\theta}\right|^2. \tag{B35}$$

Similarly, the other two cross sections are given by

$$\sigma = \frac{1}{k}\sum_l |S_l - 1|^2 = \frac{4}{k}\sum_l \sin^2\delta_l, \tag{B36a}$$

$$\sigma_{\mathrm{tr}} = \sigma - \frac{1}{k}\sum_l \Re\left[(S_l - 1)(S_{l+1}^* - 1)\right], \tag{B36b}$$

$$= \frac{2}{k}\sum_l \sin^2(\delta_{l+1} - \delta_l). \tag{B36c}$$

With the definition of $f(\theta)$ [Eq. (B33)], the underlying optical theorem can be expressed as

$$\sigma = \sqrt{\frac{8\pi}{k}}\Im\left[e^{-i\frac{\pi}{4}}f(0)\right], \tag{B37}$$

where $\Im\cdot$ denotes the imaginary part. We finally obtain the following formula for the characteristic ratio:

$$\xi = \frac{2\sum_l \sin^2\delta_l}{\sum_l \sin^2(\delta_{l+1} - \delta_l)}. \tag{B38}$$

Appendix C: Derivation of Eq. (12) or Eq. (B30)

In two dimensions, it follows from the Boltzmann transport equation that the resulting current $\boldsymbol{i}$ due to an applied electric field $\boldsymbol{E}$ takes the general form given by[66]

$$\boldsymbol{i} = \frac{ge^2}{(2\pi)^2}\int d^2\boldsymbol{k}\tau_{tr}\frac{\partial f(\epsilon)}{\partial\epsilon}(\boldsymbol{v_k}\cdot\boldsymbol{E})\boldsymbol{v}_k, \tag{C1}$$

where g denotes the degeneracies, $f(\epsilon)$ is the Fermi distribution function, and $\boldsymbol{v_k} = (1/\hbar)\nabla_{\boldsymbol{k}}\epsilon(\boldsymbol{k})$ is the band velocity. The transport relaxation time τ_{tr} can be calculated from Fermi's golden rule, which for our scattering process takes the following form in relation to the transport cross section

$$\frac{1}{\tau_{tr}} = \frac{1}{(2\pi)^2}\int d^2\boldsymbol{k'}(1-\cos\phi)W(\boldsymbol{k'},\boldsymbol{k}) = n_c v_g \sigma_{tr}, \tag{C2}$$

where n_c is the concentration of impurities and

$$W(\boldsymbol{k'},\boldsymbol{k}) = \frac{4\pi^2\hbar v_g^2 n_c}{k}|f(\phi)|^2\delta(\epsilon_{\boldsymbol{k}} - \epsilon_{\boldsymbol{k'}}) \tag{C3}$$

is the quantum scattering rate from state $|\boldsymbol{k}\rangle$ to final state $|\boldsymbol{k'}\rangle$ with the scattering angle $\phi = \arccos(\boldsymbol{k}\cdot\boldsymbol{k'}/k^2)$ and the scattering amplitude $f(\phi)$ at the angle ϕ. Comparing with the standard macroscopic equation (Ohm's law) $\boldsymbol{i} = \boldsymbol{G}\cdot\boldsymbol{E}$ with $\boldsymbol{G}$ being the conductivity tensor, we obtain, for $\boldsymbol{E} = E\boldsymbol{e}_x$,

$$G = G^{xx} = \frac{ge^2}{(2\pi)^2}\frac{1}{\hbar^2}\int_0^{2\pi}\cos^2\theta d\theta\int \epsilon d\epsilon\frac{\partial f(\epsilon)}{\partial\epsilon}\tau_{tr}. \tag{C4}$$

At zero temperature, we have

$$G = \frac{ge^2}{4\pi}\frac{\epsilon}{\hbar^2}\tau_{tr} = G_0 v_g k\tau_{tr} = G_0\frac{k}{n_c\sigma_{tr}}, \tag{C5}$$

where $g = 4$ is assumed (accounting for spin and valley) and $G_0 = 2e^2/h$ is the conductance quantum or, equivalently, the quantized unit of conductance.

* Ying-Cheng.Lai@asu.edu

[1] K. S. Novoselov, A. K. Geim, S. V. Morozov, D. Jiang, Y. Zhang, S. V. Dubonos, I. V. Grigorieva, and A. A. Firsov, Science **306**, 666 (2004).
[2] C. Berger, Z. M. Song., T. B. Li., X. B. Li, A. Y. Ogbazghi, R. F. Z. T. Dai, A. N. Marchenkov., E. H. Conrad, P. N. First, and W. A. de Heer, J. Phys. Chem. B **108**, 19912 (2004).
[3] T. Wehling, A. Black-Schaffer, and A. Balatsky, Adv. Phys. **63**, 1 (2014).
[4] J. Wang, S. Deng, Z. Liu, and Z. Liu, National Sci. Rev. (2015).
[5] M. Z. Hasan and C. L. Kane, Rev. Mod. Phys. **82**, 3045 (2010).
[6] X.-L. Qi and S.-C. Zhang, Rev. Mod. Phys. **83**, 1057 (2011).
[7] X.-L. Qi, T. L. Hughes, and S.-C. Zhang, Phys. Rev. B **78**, 195424 (2008).
[8] A. M. Essin, J. E. Moore, and D. Vanderbilt, Phys. Rev. Lett. **102**, 146805 (2009).
[9] C.-Z. Chang, W. Zhao, D. Y. Kim, P. Wei, J. K. Jain, C. Liu, M. H. W. Chan, and J. S. Moodera, Phys. Rev. Lett. **115**, 057206 (2015).
[10] Y. H. Wang, J. R. Kirtley, F. Katmis, P. Jarillo-Herrero, J. S. Moodera, and K. A. Moler, Science **349**, 948 (2015).
[11] M. C. Rechtsman, Y. Plotnik, J. M. Zeuner, D. Song, Z. Chen, A. Szameit, and M. Segev, Phys. Rev. Lett. **111**, 103901 (2013).
[12] Y. Plotnik, M. C. Rechtsman, D. Song, M. Heinrich, J. M. Zeuner, S. Nolte, Y. Lumer, N. Malkova, J. Xu, A. Szameit, Z. Chen, and M. Segev, Nat. Mater. **13**, 57 (2014).
[13] Z. Wang, Y. D. Chong, J. D. Joannopoulos, and M. Soljačić, Phys. Rev. Lett. **100**, 013905 (2008).
[14] Z. Wang, Y. Chong, J. D. Joannopoulos, and M. Soljacic, Nature (London) **461**, 772 (2009).
[15] M. Hafezi, E. A. Demler, M. D. Lukin, and J. M. Taylor, Nat. Phys. **7**, 907 (2011).

[16] K. Fang, Z. Yu, and S. Fan, Nat. Photon. **6**, 782 (2012).
[17] A. B. Khanikaev, S. H. Mousavi, W.-K. Tse, M. Kargarian, A. H. MacDonald, and G. Shvets, Nat. Mater. **12**, 233 (2013).
[18] L. Lu, J. D. Joannopoulos, and M. Soljaclc, Nat. Photon. **8**, 821 (2014).
[19] X. Huang, Y. Lai, Z. H. Hang, H. Zheng, and C. T. Chan, Nat. Mater **10**, 582 (2011).
[20] J. Mei, Y. Wu, C. T. Chan, and Z.-Q. Zhang, Phys. Rev. B **86**, 035141 (2012).
[21] P. Moitra, Y. Yang, Z. Anderson, I. I. Kravchenko, D. P. Briggs, and J. Valentine, Nat. Photon. **7**, 791 (2013).
[22] Y. Li, S. Kita, P. Munoz, O. Reshef, D. I. Vulis, M. Yin, M. Loncar, and E. Mazur, Nat. Photon. **9**, 738 (2015).
[23] A. Fang, Z. Q. Zhang, S. G. Louie, and C. T. Chan, Phys. Rev. B **93**, 035422 (2016).
[24] D. Guzmán-Silva, C. Mejía-Cortés, M. A. Bandres, M. C. Rechtsman, S. Weimann, S. Nolte, M. Segev, A. Szameit, and R. A. Vicencio, New J. Phys. **16**, 063061 (2014).
[25] S. Mukherjee, A. Spracklen, D. Choudhury, N. Goldman, P. Öhberg, E. Andersson, and R. R. Thomson, Phys. Rev. Lett. **114**, 245504 (2015).
[26] R. A. Vicencio, C. Cantillano, L. Morales-Inostroza, B. Real, C. Mejía-Cortés, S. Weimann, A. Szameit, and M. I. Molina, Phys. Rev. Lett. **114**, 245503 (2015).
[27] F. Diebel, D. Leykam, S. Kroesen, C. Denz, and A. S. Desyatnikov, Phys. Rev. Lett. **116**, 183902 (2016).
[28] S. Taie, H. Ozawa, T. Ichinose, T. Nishio, S. Nakajima, and Y. Takahashi, Sci. Adv. **1** (2015).
[29] M. Rizzi, V. Cataudella, and R. Fazio, Phys. Rev. B **73**, 144511 (2006).
[30] A. A. Burkov and E. Demler, Phys. Rev. Lett. **96**, 180406 (2006).
[31] D. Bercioux, D. F. Urban, H. Grabert, and W. Häusler, Phys. Rev. A **80**, 063603 (2009).
[32] B. Dóra, J. Kailasvuori, and R. Moessner, Phys. Rev. B **84**, 195422 (2011).
[33] A. Raoux, M. Morigi, J.-N. Fuchs, F. Piéchon, and G. Montambaux, Phys. Rev. Lett. **112**, 026402 (2014).
[34] T. Andrijauskas, E. Anisimovas, M. Račiūnas, A. Mekys, V. Kudriašov, I. B. Spielman, and G. Juzeliūnas, Phys. Rev. A **92**, 033617 (2015).
[35] F. Wang and Y. Ran, Phys. Rev. B **84**, 241103 (2011).
[36] J. Wang, H. Huang, W. Duan, and Z. Liu, The Journal of Chemical Physics **139**, 184701 (2013).
[37] W. Li, M. Guo, G. Zhang, and Y.-W. Zhang, Phys. Rev. B **89**, 205402 (2014).
[38] J. Romhanyi, K. Penc, and R. Ganesh, Nat. Commun **6** (2015), article.
[39] G. Giovannetti, M. Capone, J. van den Brink, and C. Ortix, Phys. Rev. B **91**, 121417 (2015).
[40] R. Shen, L. B. Shao, B. Wang, and D. Y. Xing, Phys. Rev. B **81**, 041410 (2010).
[41] D. F. Urban, D. Bercioux, M. Wimmer, and W. Häusler, Phys. Rev. B **84**, 115136 (2011).
[42] M. Vigh, L. Oroszlány, S. Vajna, P. San-Jose, G. Dávid, J. Cserti, and B. Dóra, Phys. Rev. B **88**, 161413 (2013).
[43] J. T. Chalker, T. S. Pickles, and P. Shukla, Phys. Rev. B **82**, 104209 (2010).
[44] J. D. Bodyfelt, D. Leykam, C. Danieli, X. Yu, and S. Flach, Phys. Rev. Lett. **113**, 236403 (2014).
[45] E. H. Lieb, Phys. Rev. Lett. **62**, 1201 (1989).
[46] H. Tasaki, Phys. Rev. Lett. **69**, 1608 (1992).
[47] H. Aoki, M. Ando, and H. Matsumura, Phys. Rev. B **54**, R17296 (1996).
[48] C. Weeks and M. Franz, Phys. Rev. B **82**, 085310 (2010).
[49] N. Goldman, D. F. Urban, and D. Bercioux, Phys. Rev. A **83**, 063601 (2011).
[50] J. Vidal, R. Mosseri, and B. Douçot, Phys. Rev. Lett. **81**, 5888 (1998).
[51] D. S. Novikov, Phys. Rev. B **76**, 245435 (2007).
[52] M. I. Katsnelson, F. Guinea, and A. K. Geim, Phys. Rev. B **79**, 195426 (2009).
[53] J.-S. Wu and M. M. Fogler, Phys. Rev. B **90**, 235402 (2014).
[54] J. Cserti, A. Pályi, and C. Péterfalvi, Phys. Rev. Lett. **99**, 246801 (2007).
[55] R. L. Heinisch, F. X. Bronold, and H. Fehske, Phys. Rev. B **87**, 155409 (2013).
[56] M. M. Asmar and S. E. Ulloa, Phys. Rev. B **87**, 075420 (2013).
[57] B. Liao, M. Zebarjadi, K. Esfarjani, and G. Chen, Phys. Rev. B **88**, 155432 (2013).
[58] M. M. Asmar and S. E. Ulloa, Phys. Rev. Lett. **112**, 136602 (2014).
[59] A. Ferreira, T. G. Rappoport, M. A. Cazalilla, and A. H. Castro Neto, Phys. Rev. Lett. **112**, 066601 (2014).
[60] Y. Zhao, J. Wyrick, F. D. Natterer, J. F. Rodriguez-Nieva, C. Lewandowski, K. Watanabe, T. Taniguchi, L. S. Levitov, N. B. Zhitenev, and J. A. Stroscio, Science **348**, 672 (2015).
[61] T. Ando, T. Nakanishi, and R. Saito, J. Phys. Soc. Jpn. **67**, 2857 (1998).
[62] W. S. Bakr, J. I. Gillen, A. Peng, S. Folling, and M. Greiner, Nature **462**, 74 (2009).
[63] D. Jin, L. Lu, Z. Wang, C. Fang, J. D. Joannopoulos, M. Soljačić, L. Fu, and N. X. Fang, arXiv:1602.00553 (2016).
[64] M. I. Katsnelson, K. S. Novoselov, and A. K. Geim, Nat. Phys. **2**, 620 (2006).
[65] E. Illes, J. P. Carbotte, and E. J. Nicol, Phys. Rev. B **92**, 245410 (2015).
[66] J. Ziman, *Principles of the Theory of Solids* (Cambridge University Press, 1972).